Inorganic Chemistry

pubs.acs.org/IC

Article

Evaluation of P3-Type Layered Oxides as K-Ion Battery Cathodes

Pawan Kumar Jha, Sanyam Nitin Totade, Prabeer Barpanda, and Gopalakrishnan Sai Gautam*

Cite This: *Inorg. Chem.* 2023, 62, 14971−14979

Read Online

ACCESS | Metrics & More | Article Recommendations | Supporting Information

ABSTRACT: Given the increasing energy storage demands and limited natural resources of Li, K-ion batteries (KIBs) could be promising next-generation systems having natural abundance, similar chemistry, and energy density. Here, we have investigated the P3-type $K_{0.5}TMO_2$ (where TM = Ti, V, Cr, Mn, Co, or Ni) systems using density functional theory calculations as potential positive intercalation electrodes (or cathodes) for KIBs. Specifically, we have identified ground-state configurations and calculated the average topotactic voltages, electronic structures, on-site magnetic moments, and thermodynamic stabilities of all P3-$K_{0.5}TMO_2$ compositions and their corresponding depotassiated P3-TMO_2 frameworks. Additionally, we evaluated the dynamic stability and K-mobility in select P3 structures. We find that K adopts the honeycomb or zig-zag configuration within each K-layer of all P3 structures considered, irrespective of the transition-metal (TM). In terms of voltages, we find the Co- and Ti-based compositions to exhibit the highest (4.59 V vs. K) and lowest (2.24 V) voltages, respectively, with the TM contributing to the redox behavior upon K (de-)intercalation. We observe all P3-$K_{0.5}TMO_2$ to be (meta)stable and hence experimentally synthesizable according to our 0 K convex hull calculations, while all depotassiated P3-TMO_2 configurations are unstable and may appear during electrochemical cycling. Also, we verified the stability of the prismatic coordination environment of K compared to octahedral coordination at the $K_{0.5}TMO_2$ compositions using Rouxel and cationic potential models. Finally, combining our voltage and stability calculations, we find P3-K_xCoO_2 to be the most promising cathode composition, while P3-K_xNiO_2 is worth exploring. We also find P3-K_xMnO_2 to be worth pursuing given its dynamic stability and facile migration of K^+ at both potassiated and depotassiated compositions. Our work should contribute to the exploration of strategies and materials required to make practical KIBs.

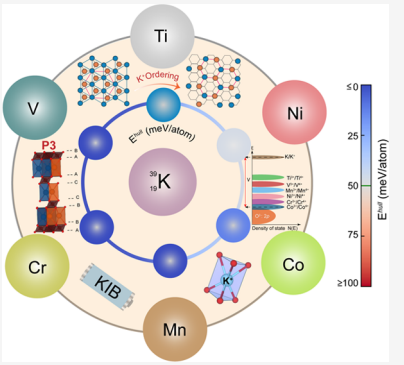

INTRODUCTION

Lithium-ion batteries (LIBs) have played a preeminent role in energy storage for the last three decades.[1−3] However, our excessive dependence on LIBs raises several challenges on natural abundance of critical elements, fragile supply chains, and cost,[4] which has motivated the search for intercalation chemistries that can be an alternative to LIBs. Notably, K-ion batteries (KIBs) have emerged as a viable alternative for economic grid-scale storage applications owing to the natural abundance of K, reversible (de)intercalation into graphite (as anode), and lower standard redox potential (K/K^+, −2.936 V vs. standard hydrogen electrode—SHE).[5−7] Despite several advantages over Li (and Na), the practical development of KIB is constrained by the need for robust cathode materials that can (de)intercalate K^+ reversibly. Several classes of materials have been explored as K-intercalation cathodes, namely, layered oxides, polyanionic frameworks, Prussian blue analogous, and organic compounds.[5] Out of these, layered transition-metal oxides (TMOs), similar to those used for Li and Na (de)intercalation, are promising in terms of their high theoretical energy density, high rate capability owing to the large two-dimensional K^+ diffusion pathways, and possible structural stability during cycling due to the large slab spacing that can suppress detrimental transition-metal (TM) migration into K-layers.[8]

Typical K-containing layered structures, of composition K_xTMO_2 ($x \leq 1$, TM = transition metal), exhibit a variety of stacking sequences, including prismatic-based P3 or P2, and octahedral-based O3 or O2, where the P3, P2, O3, and O2 notations are defined as per the nomenclature of Delmas and co-workers.[9] The type of coordination environment preferred by K (i.e., octahedral vs. prismatic; see Figure S1 for an illustration) in a given framework, which in turn determines the type of stacking sequence of the structure, is primarily determined by the TM itself, the oxidation state(s) of the TM, and the K-concentration. For example, $KScO_2$ and $KCrO_2$ exhibit the O3 framework, while $K_{0.5}MnO_2$ adopts the P3 framework.[10−15] The relative stability of octahedral and prismatic coordination can also be quantified via the "cationic potential" model and/or the Rouxel diagram.[9,16] Notably, prismatic coordination is often stabilized at intermediate ($x \sim 0.5$) or nonstoichiometric ($x < 1$) K-concentrations in layered frameworks, similar to observations in analogous Na-

Received: May 23, 2023
Published: September 7, 2023

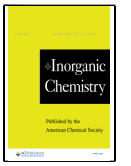

containing layered systems,[17−20] as illustrated by K_xCrO_2, K_xMnO_2, and K_xCoO_2 systems.[11,19] Indeed, Hagenmuller and co-workers' experiment-derived phase diagram of A_xMO_2 (A = Na or K; M = Cr, Mn, or Co) indicates that either P3 or P′3 is the stable phase at intermediate Na- or K-concentrations, irrespective of the TM.[11]

Experimentally, stoichiometric $KTMO_2$ (x = 1) has been synthesized only in K_xScO_2, K_xCrO_2, K_xFeO_2, and K_xMnO_2 systems, with limitations on the observable electrochemical capacity.[10−15] As a result, previous studies have investigated nonstoichiometric K_xTMO_2 frameworks, often dealing with prismatic phases. For example, Vaalma et al. demonstrated $K_{0.3}MnO_2$ as a possible K-intercalation host,[21] which was followed by Kim et al.'s report that found P3-$K_{0.5}MnO_2$ as a viable candidate as well.[22] Interestingly, the analogous P3-Na_xMnO_2 compound is metastable and cannot be trivially synthesized.[23,24] Hironaka et al. showed P3-K_xCoO_2 as an efficient reversible K-intercalation host,[25] while Hwang et al. developed P3-$K_{0.69}CrO_2$ *via* electrochemical ion exchange from the parent O3-$NaCrO_2$ compound.[26] Notably, previous computational studies have revealed that the diffusivity of K^+ in prismatic stacking is higher than in octahedral stacking.[24,26,27] Thus, the existing literature indicates that K-containing layered TMOs with prismatic stacking sequences can be easily synthesized and exhibit reasonable cyclability and good rate performance. However, systematic computational or experimental studies of P3-type K-containing layered TMOs are missing so far.

Here, we have used density functional theory (DFT[28,29]) calculations to systematically evaluate various K-ion-containing P3-layered oxides as candidate electrodes for KIBs. Specifically, we have calculated the lattice parameters, average intercalation voltage, thermodynamic stability, electronic properties, and on-site magnetic moments in K_xTMO_2 systems, where TM = Ti, V, Cr, Mn, Co, or Ni. For the Mn analogue, we have evaluated the dynamic stability and K-mobility as well. We enumerate the possible in-plane K-ion orderings for $K_{0.5}TMO_2$ compositions and determine the ground states using DFT. Subsequently, we evaluate the aforementioned properties for the ground-state $K_{0.5}TMO_2$ configuration and its corresponding depotassiated composition, namely, TMO_2. Notably, we observe that all P3-type $K_{0.5}TMO_2$ systems are thermodynamically stable, except V and Cr, with Co (Ti) system exhibiting the highest (lowest) predicted voltage of 4.59 V (2.24 V) vs. K. The ground-state configurations for all $K_{0.5}TMO_2$ systems are identical, with K exhibiting a honeycomb or zig-zag ordering in each K-layer. Based on calculated projected density of states (pDOS) and on-site magnetic moments, we expect the TM to be redox-active upon K (de)intercalation in P3-K_xTMO_2. Also, we demonstrate the stability of prismatic over octahedral coordination in the $K_{0.5}TMO_2$ systems considered, via the Rouxel and cationic potential model approaches. Finally, based on voltage and stability metrics, we expect P3-K_xCoO_2 and K_xNiO_2 to be promising candidates, while the dynamic stability and facile K-mobility also make K_xMnO_2 worth considering. We hope that our study will reinvigorate the computational and experimental investigations of P3-K_xTMO_2 systems as K-intercalating hosts.

COMPUTATIONAL METHODS

We used the Vienna Ab Initio Simulation Package[30−32] to perform the DFT calculations using the plane wave basis set with a kinetic energy cut-off of 520 eV and the projector augmented wave (PAW[32,33]) potentials to model the ionic cores, consistent with our previous works.[34,35] We sampled the irreducible Brillouin zone using Γ-centered Monkhorst−Pack[36] k-point meshes with a density of 32 points per Å, and we integrated the Fermi surface with a Gaussian smearing of width 0.05 eV. We relaxed the cell volume, shape, and ionic positions of all our structures without any symmetry constraints till the atomic forces and the total energy were converged within |0.05| eV/Å and 10^{-5} eV, respectively.[37] For describing the electronic exchange correlation, we utilized the Hubbard U corrected, strongly constrained, and appropriately normed (SCAN[38]) functional, i.e., SCAN + U. As derived in previous works, we used Hubbard U corrections[39] of 2.5, 1.0, 2.7, 3.0, and 2.5 eV for Ti, V, Mn, Co, and Ni, respectively.[34,35] All pDOS calculations were done with the "fake-self-consistent-field" procedure, as detailed in previous works.[40,41]

All our calculations were spin-polarized, and we initialized the magnetic moments of all TM metals in a high-spin ferromagnetic (FM) ordering, except Co and Ni where we initialized with a low-spin ferromagnetic ordering for both the +3 and +4 oxidation states. For the $K_{0.5}TMO_2$ structures, we arbitrarily initialized the magnetic moments of half of the TMs as +3 and the other half as +4, respectively. To test whether an arbitrary initialization of magnetic moment magnitudes leads to different (i.e., not ground state) configurations, we initialized all of the Mn in P3-$K_{0.5}MnO_2$ with a +5 magnetic moment (which corresponds to a high-spin configuration of Mn^{2+}). Importantly, we observed that our structure relaxation yielded the same Mn with +3 and +4 oxidation states, as compared to our normal strategy of arbitrarily assigning half the Mn as +3 and the other half as +4. To examine the influence of magnetic orderings, we calculated and compared the total energies of a low-spin antiferromagnetic (AFM), a high-spin FM, and a low-spin FM configuration in P3-$K_{0.5}CoO_2$ (Table S1). Notably, we observed the low-spin FM configuration to be stable compared to the AFM (by ∼200 meV/fu) and the high-spin FM (by ∼500 meV/fu) configurations, highlighting that our choice of a low-spin FM initialization led to the precise ground state in the case of Co. While the initial assignment of FM vs. AFM ordering does play a role in the eventual total energy during structure relaxation of P3-$K_{0.5}TMO_2$, we believe that the initial charge ordering (i.e., +3 and +4 oxidation-state assignment) does not play an important role during relaxation.

The starting structure for Ti, V, Mn, and Ni $K_{0.5}TMO_2$ compositions was P3-$K_{0.3}MnO_2$, as obtained from the inorganic crystal structure database (ICSD[42]), where we created Ti, V, and Ni structures via ionic substitution of Mn in P3-$K_{0.3}MnO_2$. We constructed the Cr- and Co-based structures based on previous reports.[10,25] Since several K-vacancy configurations are possible at the target $K_{0.5}TMO_2$ composition, we used the pymatgen package to enumerate all symmetrically distinct orderings[43] within each K_xTMO_2 supercell of size 2 × 2 × 1. There are 12 formula units of P3-$K_{0.5}TMO_2$ (or P3-TMO_2) present in the supercells considered, which correspond to 42 (36) atoms. We used VESTA for the visualization and illustration of structures used in our calculations.[44]

The redox reaction of topotactic (de-)intercalation of K^+ in a P3-type TMO_2 can be represented as

$$yK^+ + ye^- + K_{0.5-y}TMO_2 \rightarrow K_{0.5}TMO_2 \quad (1)$$

where $K_{0.5}TMO_2$ and $K_{0.5-y}TMO_2$ represent the potassiated and depotassiated structures, respectively. The average intercalation voltage can be calculated via the Nernst equation from the difference in Gibbs energies (G) of the potassiated and depotassiated compositions. We approximated the Gibbs energies with the DFT-calculated total energies (i.e., $G \approx E$), thus ignoring the p-V and entropic contributions.[45,46] Within this approximation and with F being the Faraday's constant, the average K-intercalation voltage vs. K/K^+ is

$$V = \frac{-(E_{K_{0.5}TMO_2} - E_{K_{0.5-y}TMO_2} - yE_K)}{y \cdot F} \quad (2)$$

https://doi.org/10.1021/acs.inorgchem.3c01686
Inorg. Chem. 2023, 62, 14971−14979

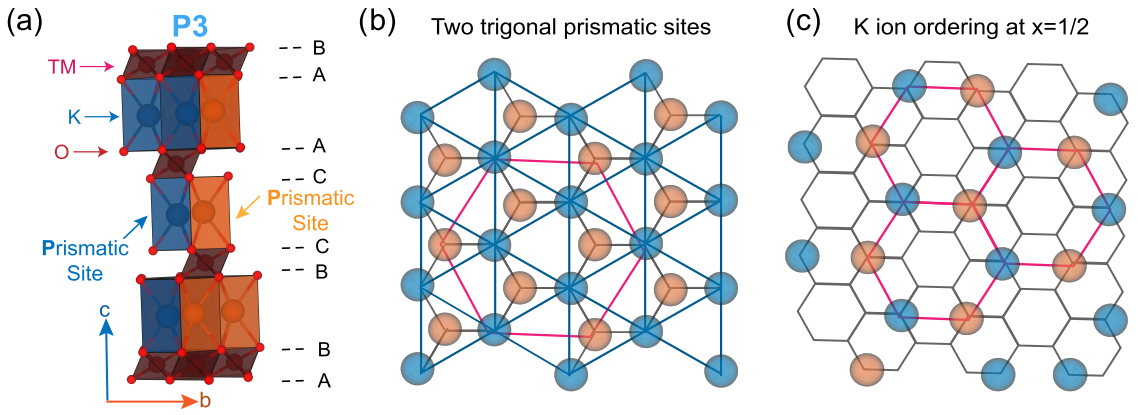

Figure 1. (a) Unit cell of typical P3-K_xTMO_2 structure. (b) Visualization of different types of prismatic sites (blue and orange spheres) that are available for K-occupation, per K-layer in P3-K_xTMO_2. The blue and orange spheres are equivalent to the blue and orange polyhedra shown in panel (a). (c) Honeycomb or zig-zag ordering in each K-layer that constitutes the ground-state configuration for all P3-$K_{0.5}TMO_2$ considered. Pink guidelines in panels (b) and (c) connect identical K-sites.

where $E_{K_{0.5}\ TMO_2}$, $E_{K_{0.5-y}\ TMO_2}$, and E_K are the DFT-calculated total energies of the ground-state potassiated configuration, depotassiated composition, and the body-centered cubic phase of pure K, respectively.

In order to assess the thermodynamic stability of P3-type $K_{0.5}TMO_2$ and TMO_2 compositions, we computed the 0 K phase diagram (or the convex hull) of each ternary K−TM−O system based on the DFT-calculated total energies of all elements, and compounds (i.e., binary and ternaries), whose experimentally reported structures are available in the ICSD. We used the pymatgen package to construct the phase diagrams.[43] Note that the collection of thermodynamically stable phases at a given temperature forms a "convex hull" of the chemical space at that temperature. We quantify the instability (stability) of $K_{0.5}TMO_2$ and TMO_2 by calculating the energy above (below) the hull, denoted by E^{hull}, based on 0 K phase diagrams.[43,47−49] The energy above the hull (or positive E^{hull}) refers to the largest decomposition energy that can be obtained as a metastable or unstable compound transitions into a stable compound(s). In the case of energy below the hull (or negative E^{hull}), we quantify the lowest formation energy that can be obtained as a stable compound form from other stable compound(s) in its chemical space.[47] Note that we used a $E^{hull} \leq 50$ meV/atom as a threshold value for a structure being experimentally synthesizable, but this threshold is arbitrary and is highly chemistry-dependent.[49] A E^{hull} of 50 meV/atom corresponds to a thermal energy at a temperature of ∼580 K.

We used the phonopy package and SCAN + U functional to perform phonon density of states (DOS) calculations to determine the dynamic stability and thermal properties of P3-$K_{0.5}MnO_2$ and P3-MnO_2 structures.[50] From the symmetrically different displacements of magnitude 0.01 Å of all of the atoms within each supercell (42 or 36 atom cells, as described above), we obtained the necessary force constants. Using a convergence threshold of 10^{-6} eV on the total energies, we performed a self-consistent field calculation for all of the atomic displacements considered by sampling the irreducible Brillouin zone only at the Γ point. Finally, we used a 24 × 24 × 24 mesh to sample the phonon frequencies and thermal properties, as displayed in Figures S6 and S7, respectively.

To quantify the mobility of K-ion in a P3 structure, we have used the nudged elastic band (NEB[51]) framework in conjunction with DFT to calculate the migration barrier (E_m) and the minimum energy pathway for a K^+ migration in P3-MnO_2. Specifically, we considered the migration of an isolated K^+ across adjacent equivalent prismatic sites in P3-$K_{0.5}MnO_2$ and P3-MnO_2, i.e., at concentrated and dilute K-limits (see Figure S8b for an illustration). The migration path was modeled using 7 images that were held together by spring forces of 5 eV/Å, and we converged the band forces till their magnitudes fell below |0.05| eV/Å. We used the SCAN functional for the NEB calculation, based on our previous study[52] that has shown that SCAN provides more accurate E_m on average. For the initial and final end-point images, we subsequently relaxed them with SCAN. Convergence criteria for both end-point relaxations are 10^{-5} eV on total energies and |0.01| eV/Å on the atomic forces.

RESULTS

Structure, K-Ordering, and Lattice Parameters. Figure 1a illustrates the typical unit cell of P3-K_xTMO_2, consisting of three TMO_2 layers, denoted by the brown polyhedra. The topologically distinct prismatic sites of K are shown by blue and orange polyhedra in Figure 1a and equivalently by blue and orange spheres in Figure 1b. Combined, the two prismatic sites arrange themselves in a hexagonal lattice, as shown by the black guidelines in panels b and c of Figure 1. Each KO_6 prism shares one of its triangular faces with one TMO_6 octahedra, thus violating the third Pauling's rule,[53,54] while the other triangular face shares its three edges with three different TMO_6 octahedra. The oxygen packing in P3 compounds follows the ABBCCA sequence.

The K-vacancy arrangement in each K-layer is an optimization of the steric and electrostatic interactions between the K-ions for any $K_{0.5}TMO_2$. Interestingly, we found the ground-state K-vacancy configuration of all K_xTMO_2 systems to be identical, as indicated in Figure 1c by the honeycomb or zig-zag ordering of K^+ in each K-layer. Specifically, in each of the blue + orange hexagon of Figure 1b, K^+ occupies the farthest possible combination of one blue and one orange site, resulting in the honeycomb ordering of Figure 1c. This is equivalent to a K−K distance of 2a if the side-length of the hexagon in Figure 1b is a. Also, our in-plane K-ordering is similar to previous experimental and theoretical studies,[55−58] with marginal differences in the construction of the honeycomb ordering. Note that the scale of panels (b) and (c) in Figure 1 are different, where the pink guidelines in both panels connect identical set of K-sites.

The SCAN + U-calculated lattice parameters for the ground-state configurations of all $K_{0.5}TMO_2$ systems considered are compiled in Table S2. The computed lattice parameters are in good agreement with available experimental values,[22,25,26] with the maximum overestimation (underestimation) of the c parameter of 4.69% (2.79%). Increase in the atomic number of the TM monotonically decreases the a and b lattice parameters (see trendlines in Figure 2a), caused primarily by a

https://doi.org/10.1021/acs.inorgchem.3c01686
Inorg. Chem. 2023, 62, 14971−14979

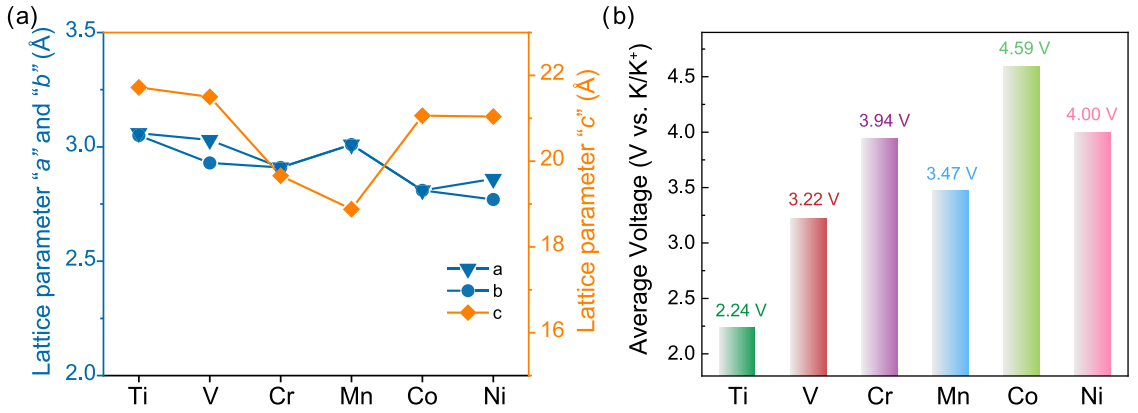

Figure 2. SCAN + *U*-calculated (a) lattice parameters in various $K_{0.5}TMO_2$ systems and (b) average K-intercalation voltage across the different $K_{0.5}TMO_2$-TMO_2 compositions. Average voltage values in panel (b) are also indicated by text annotations.

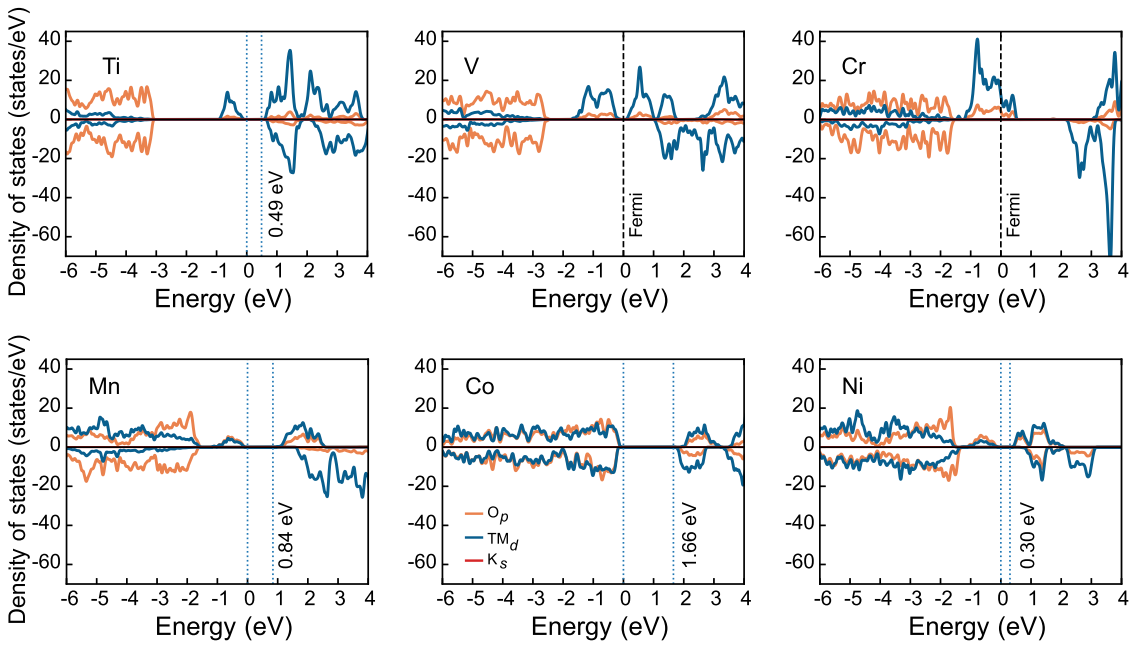

Figure 3. SCAN + *U*-calculated pDOS for all P3-$K_{0.5}TMO_2$ systems. Blue, orange, and red curves correspond to TM *d*, O *p*, and K *s* states. Positive (negative) values of pDOS correspond to up (down) spin electrons. Dotted blue lines represent the valence and conduction band edges (CBEs), with the numbers indicating band gap values. Dashed black lines signify the Fermi level. The zero on the energy scale in each panel is referenced either to the valence band maximum or to the Fermi level.

decrease in TM−O bonds, except for Mn and Ni, which can be attributed to the Jahn−Teller distortion of Mn^{3+} and Ni^{3+} (Figure S2). As shown in Figure 2a and Table S2, the Jahn−Teller distortion also causes a decrease in the *c* parameter for Mn compared to Cr and Co, whereas in Ni, the *c* parameter remains similar to Co.

Average Voltages. Figure 2b presents the calculated average topotactic intercalation voltage, referenced against K/K^+, for the P3-type $K_{0.5}TMO_2$-TMO_2 systems considered in this work. Notably, the predicted voltages range from 2.24 V for the $K_{0.5}TiO_2$-TiO_2 system to 4.59 V for the $K_{0.5}CoO_2$-CoO_2 system, which is within the stable window of typical electrolytes used for KIBs.[5] The calculated intercalation voltage increases progressively as we move from Ti to Co, in accordance with the standard reduction potentials of the corresponding TMs, as noted in a previous study.[40] Importantly, Mn and Ni systems show markedly lower voltages compared to their neighboring TMs, which can be partly attributed to Jahn−Teller distortions of Mn^{3+} and Ni^{3+}. Note that Jahn−Teller distortions typically tend to destabilize discharged phases compared to charged phases, especially when the charged phases have TMs in +4 oxidation states, causing a drop in the average intercalation voltage. Also, the predicted voltage drop from Co to Ni is similar to the observation in Li-containing layered oxides, caused by the filling of the antibonding e_g orbital of NiO_2.[40] Finally, the lower intercalation voltage of 2.24 V for the K_xTiO_2 system suggests that this system can be explored as an anode for KIBs.

Electronic Structure and Magnetic Moments. The calculated pDOS of all $K_{0.5}TMO_2$ ground-state structures are displayed in Figure 3, with Figure S3 compiling the pDOS of all TMO_2 structures. The red, blue, orange, dotted blue, and dashed black lines represent K *s* states, O *p* states, TM *d* states, band edges, and Fermi level, respectively, with the numbers in each panel indicating band gaps. Except $K_{0.5}CrO_2$, $K_{0.5}VO_2$, and CrO_2, all $K_{0.5}TMO_2$ and TMO_2 structures are predicted to

https://doi.org/10.1021/acs.inorgchem.3c01686
Inorg. Chem. 2023, 62, 14971−14979

be semiconductors by SCAN + U. The calculated band gaps exhibit a non-monotonic trend as we move along the 3d series in $K_{0.5}TMO_2$, decreasing from 0.49 eV in Ti to 0 eV in Cr, subsequently increasing up to 1.66 eV in Co and further decreasing to 0.30 eV in Ni. Band gap trends in TMO_2 structures (Figure S3) are similar to $K_{0.5}TMO_2$, with the gap decreasing from 2.85 to 0 eV from Ti to Cr, then increasing to 2.40 eV in Mn and finally decreasing to 1.39 eV in Ni.

While TM d states dominate the valence band edge (VBE) or the Fermi level in Ti, V, and Cr versions of $K_{0.5}TMO_2$ (Figure 3), both O p and TM d states contribute equally in the case of Mn, Co, and Ni analogues, attributed to increased hybridization of the TM−O bonds as we move across the 3d series. In the case of conduction band edges (CBEs), the TM d states dominate from Ti to Mn, while O p states contribute significantly alongside TM d states in Co and Ni structures. In the case of depotassiated-TMO_2 structures (Figure S3), O p states dominate the VBE in TiO_2, CoO_2, and NiO_2, TM d states dominate VBE in VO_2, while a mixture of O p and TM d states contribute to the VBE/Fermi level in MnO_2 and CrO_2. The CBE of TMO_2 structures are dominated by TM d states, with the exception of NiO_2, where a mixture of O p and Ni d states contribute.

Given that TM d states contribute significantly to the VBE/Fermi level (responsible for oxidation) of all $K_{0.5}TMO_2$ and the CBE/Fermi level (responsible for reduction) of all TMO_2 structures (except NiO_2), we expect the TM to be predominantly redox-active during K^+ (de)intercalation across all P3 systems (with Ni being a possible exception). Note that O p states are known to contribute to the redox activity in other reported high-voltage Ni-containing compounds, such as $K_2Ni_2TeO_6$.[59] Also, we observe that O p states contribute to a larger extent to the VBE as K is removed across all $K_{0.5}TMO_2$ structures (i.e., comparing Figures 3 and S3). This signifies that not only the Fermi energies shift as K is removed from (added to) $K_{0.5}TMO_2$ (TMO_2) but also the nature of the VBEs change due to the push of the unoccupied (occupied) TM d states to the CBE (VBE).

To further probe the possible origins of redox activity in the P3 frameworks, we analyzed the calculated on-site magnetic moments of the TM in each system, as tabulated in Table S3. In all ground-state $K_{0.5}TMO_2$ configurations, we observe that half the TM ions are in 3+, and the rest in 4+ oxidation states, except $K_{0.5}CrO_2$, where the d electrons appear delocalized across Cr centers due to their metallic nature. Upon K-removal, all of the transition metals in all TMO_2 structures are in a uniform 4+ oxidation state, as suggested by the calculated magnetic moments (see Table S3), highlighting that the TM exclusively contributes to the redox activity with K^+ (de)-intercalation. Also, we observe from the magnetic moments that each K^+ in $K_{0.5}TMO_2$ shares the triangular face with a TM^{4+} octahedra and the triangular edges with three TM^{3+} octahedra.

Thermodynamic Stability. The E^{hull} for the $K_{0.5}TMO_2$ and TMO_2 compositions are displayed as a heatmap in Figure 4, where blue (red) tiles indicate compositions that are stable (unstable). The solid green line across the legend bar in Figure 4 signifies the 50 meV/atom stability threshold. The 0 K convex hulls of K−TM−O ternaries (relevant for potassiated compositions) and TM−O binaries (relevant for depotassiated compositions) are compiled in Figures S4 and S5, respectively. Importantly, the E^{hull} data indicates high degree of stability for all $K_{0.5}TMO_2$ frameworks, with the exception of $K_{0.5}VO_2$ and $K_{0.5}CrO_2$, which are metastable with E^{hull} of 47 and 13 meV/atom, respectively, below the 50 meV/atom threshold. Thus, we expect all P3-type potassiated compositions considered in this work to be experimentally synthesizable.

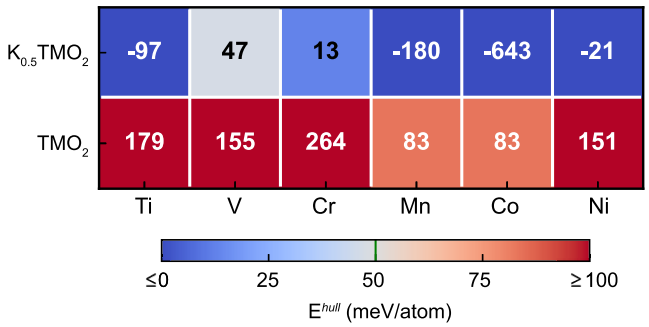

Figure 4. DFT-calculated E^{hull} for P3-$K_{0.5}TMO_2$ (top row) and P3-TMO_2 (bottom row) compositions. Each column represents a given TM. Blue (red) squares indicate high degrees of stability (instability), with the specific E^{hull} value of each composition listed as a text annotation in the corresponding square. The green line on the legend bar indicates the rule-of-thumb E^{hull} ~ 50 meV/atom threshold for experimental synthesizability.

In the case of depotassiated compositions, we find all P3-TMO_2 structures to be unstable, with E^{hull} more than 50 meV/atom. Thus, we do not expect the synthesis of P3-TMO_2 configurations to be facile. However, during electrochemical cycling, the P3-TMO_2 structures may exist in a metastable manner, due to kinetic barriers to transform to the corresponding stable states. Notably, the lower extent of instability displayed by P3-CoO_2 and P3-MnO_2 (E^{hull} ~ 83 meV/atom) is more promising than the other frameworks in terms of their ability to appear during electrochemical cycling and not decompose to other stable compositions. Finally, combining both stability and voltage metrics, we find P3-K_xCoO_2 to be the most promising cathode composition, while P3-K_xNiO_2 can also be explored as a candidate.

Dynamic Stability and K-Mobility. To assess the dynamic stability of K-containing P3 frameworks, we considered the case of P3-$K_{0.5}MnO_2$ and P3-MnO_2, where we calculated the phonon density of states (DOS) and the associated thermal properties (as compiled in Figures S6 and S7). Importantly, we observe no significant imaginary frequencies in either the potassiated or the depotassiated compositions, indicating that the compounds are dynamically stable. Note that the minor imaginary mode that we do observe in $K_{0.5}MnO_2$ is likely due to numerical noise in our calculations. Given that an unstable/metastable structure can be dynamically stable, as illustrated by our example of P3-MnO_2 (E^{hull} ~ 83 meV/atom, Figure 4), we believe that using the 0 K thermodynamic stability as a filtering criterion is more robust in identifying possible new materials.

Further, we considered the P3-$K_{0.5}MnO_2$ and P3-MnO_2 structures as a candidate framework for evaluating K-mobility at the pristine and dilute K-limits (i.e., an one K-migrating within the structure). Importantly, we calculate E_m of 125 and 147 meV for K^+ in $K_{0.5}MnO_2$ and MnO_2, respectively (Figure S8), which indicates facile K^+-transport at 298 K.[60] Thus, given the structural similarities across the P3 frameworks considered, we do not expect P3 structures to exhibit significant mobility bottlenecks as K-ion cathodes.

https://doi.org/10.1021/acs.inorgchem.3c01686
Inorg. Chem. 2023, 62, 14971−14979

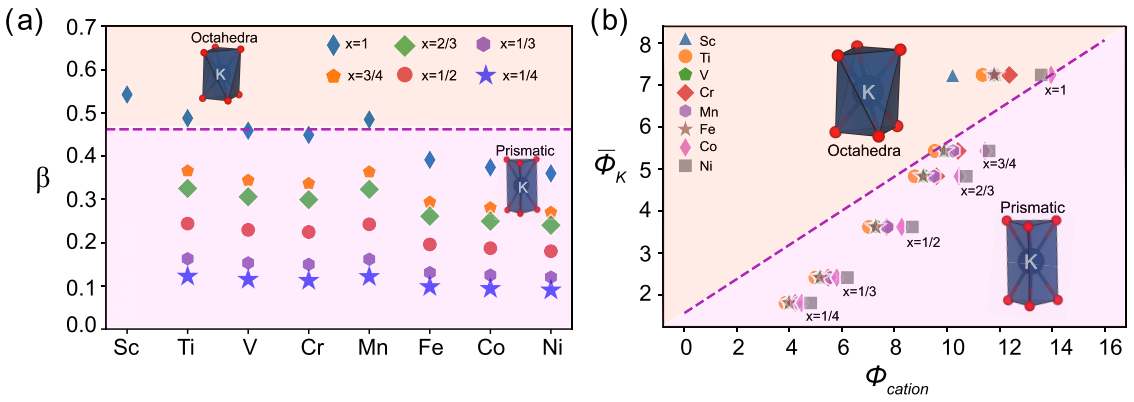

Figure 5. (a) Rouxel diagram and (b) cationic potential phase map for various K_xTMO_2 compositions. The dashed line in both panels separates the region of stability of octahedral-coordinated phases from prismatic-coordinated phases. Each column of data points in panel (a) represents a distinct TM, while the symbols represent various K compositions (x). In panel (b), each row of data points corresponds to a unique x, while the symbols distinguish the TMs.

DISCUSSION

Using DFT-based calculations, we have explored the P3-$K_{0.5}TMO_2$ frameworks as potential intercalation hosts for KIBs in this work. Specially, we have computed the lattice parameters, ground-state K-vacancy configurations, average K-interaction voltage, electronic structure, on-site magnetic moments, and 0 K thermodynamic stability for P3-$K_{0.5}TMO_2$ and the corresponding depotassiated-TMO_2 structures, where TM is Ti, V, Cr, Mn, Co, or Ni. We found that all $K_{0.5}TMO_2$ ground states adopted the honeycomb or zig-zag ordering of K-ions. With respect to voltage predictions, we observed the highest (lowest) voltages to arise from the Co (Ti) system, consistent with trends in standard reduction potentials. While we found all potassiated P3-$K_{0.5}TMO_2$ compositions to be stable or metastable (i.e., $E^{hull} \leq 50$ meV/atom), highlighting experimental synthesizability, all depotassiated P3-TMO_2 compositions were unstable, indicating that they may not be synthesizable experimentally but may appear during electrochemical cycling due to kinetic barriers for decomposition. Notably, we found both P3-$K_{0.5}MnO_2$ and P3-MnO_2 to be dynamically stable, indicating that 0 K thermodynamic (in)stability is a more robust screening metric. Also, we observed the TM to be the primary participant in the redox process, characterized by the electronic structure and on-site magnetic moments of the potassiated and depotassiated compositions. Finally, combining voltage and stability metrics, we find the P3 frameworks of K_xCoO_2 and K_xNiO_2 to be promising cathode candidates, while P3-K_xTiO_2 may be explored as an anode. Given the facile K^+ mobility in P3-$K_{0.5}MnO_2$ and P3-MnO_2, we suggest that the P3-K_xMnO_2 framework is also worth exploring.

Typically, in layered oxide frameworks, K can occupy either prismatic or octahedral coordination (Figure S1), depending on the K-concentration, and associated steric and electrostatic interactions within the structure. The relative stability of the prismatic vs. octahedral coordination environment of K (and hence the stacking sequence of the layered structure) can be modeled via the modified Rouxel diagram[9] and the cationic potential[16] phase map, which are displayed in panels (a) and (b) of Figure 5, respectively. Numerical details of the Rouxel diagram and cationic potential frameworks are described in the Supporting Information (SI), with Tables S4−S7 compiling relevant parameters or values.

In the Rouxel diagram framework, the critical parameter (β) is used as a classifier of prismatic and octahedral phases (see formulation provided in the SI). β depends on the ionic or covalent nature of the bonds between the cations (K and TM) and anions (O), and the K-concentration (x). Figure 5a plots β at different K compositions (x = 1/4, 1/3, 1/2, 2/3, 3/4, and 1) as the TM is varied in K_xTMO_2. Importantly, we observe that all $K_{0.5}TMO_2$ compositions prefer prismatic coordination, while several $KTMO_2$ compositions (except $KScO_2$, $KTiO_2$, and $KMnO_2$) also favor the prismatic coordination for any K content.

Cationic potential (ϕ_{cation}) is a descriptor of interslab interactions, i.e., the higher the cationic potential of a metal, the higher the ionic polarizability and more covalent the bond between the metal and an anion. The higher cationic potential also indicates stronger repulsion between adjacent TMO_2 octahedra (resulting from larger electrostatic repulsion of higher oxidation-state metals) and weaker interaction between adjacent KO_2 slabs. The larger interlayer distance in a prismatic structure usually coincides with a higher cationic potential implying more covalent TM−O bonds. Conversely, the smaller interlayer distances in O3 structures (at similar compositions as corresponding P3 structures) coincide with a lower cationic potential.

Apart from interlayer distances, ϕ_{cation} is also dependent on K-concentration. For example, at low x in K_xTMO_2 (or equivalently lower mean ionic potential of K, $\overline{\phi}_K$), binding of TMO_2 layers by K via electrostatic attraction between K^+ and O^{2-} is weaker, resulting in larger interlayer spacings and prismatic stacking, which is what we observe in Figure 5b. Additionally, variations in $\overline{\phi}_K$ and ϕ_{cation} for various K_xTMO_2 compositions indicate that prismatic structures should be observed at x = 1/2 for all TM, consistent with the Rouxel diagram framework as well (Figure 5a). Trends in panels (a) and (b) of Figure 5 are also in agreement with the literature reported so far for K-based layered oxides,[5] highlighting the utility of such empirical frameworks. Additionally, ϕ_{cation} can be tuned by the addition/doping of multiple TMs within the same layered oxide, thereby stabilizing either octahedral or prismatic coordination for the K-ions.

We find the honeycomb or zig-zag arrangement of K^+ to be the ground-state configuration of all $K_{0.5}TMO_2$ compositions, as displayed in Figure 1c. Owing to the larger size and higher ionicity of K^+, there is strong in-plane electrostatic and steric

https://doi.org/10.1021/acs.inorgchem.3c01686
Inorg. Chem. 2023, 62, 14971−14979

repulsion that tends to maximize the K^+−K^+ distance, irrespective of the TM. Thus, K^+ can be considered to effectively screen TM−TM interactions across the layers (at x = 0.5), which can be a cause of our observation of identical $K_{0.5}TMO_2$ ground states. Additionally, we find that each K^+ shares its triangular face and three triangular edges with TM^{4+} and TM^{3+}, respectively, which may be a result of electrostatic interactions as well. Another consequence of the large size and higher ionicity of K^+ is the observed lower intercalation voltages than analogous Na-layered compounds, despite K/K^+ exhibiting a more negative standard reduction potential than Na/Na^+.[5,40,61] Specifically, the stronger electrostatic interactions between the K^+ and TM ions can result in increasing the interlayer distance and could weaken the TM−O bonds by increasing the TM−O bond lengths compared to Na analogues.[62]

While we have used the SCAN + U framework for describing the electronic exchange and correlation, recent studies have reported that SCAN + U overestimates average voltages in Li-intercalation electrodes.[40,41] Indeed, we observe a similar overestimation of average voltages in P3-K_xCrO_2, K_xMnO_2, and K_xCoO_2, where our predicted values are ∼3.94, ∼3.47, and ∼4.59 V vs. K, respectively (Figure 2b), compared to the experimental ∼2.7 V in Cr (cathode composition was $K_{0.69}CrO_2$), ∼2.7 V in Mn ($K_{0.5}MnO_2$), and ∼3.1 V in Co ($K_{2/3}CoO_2$).[22,25,26] Such overestimation of voltages may arise from an underestimation of energies (i.e., total DFT-calculated energies are less negative) of metastable/unstable phases, such as depotassiated-TMO_2 structures.[40] Note that all our calculated voltages, despite being overestimated by SCAN + U, are within the stability window of the commonly used electrolyte, KPF_6 in ethylene carbonate:diethyl carbonate.

Finally, when it comes to phase stability, SCAN + U frequently does not provide quantitative precision owing to underestimation of total energies of metastable phases. Yet, our calculations predict that the traditional chemical synthesis pathway can produce P3- $K_{0.5}TMO_2$, owing to the calculated (meta)stability of P3-$K_{0.5}TMO_2$, whereas the depotassiated P3-TMO_2 may appear during electrochemical cycling. However, there are several phases that can be accessed, in a metastable fashion, in electrochemical setups, due to kinetic barriers that may exist for transitioning into the ground state. Thus, we believe that synthesizing the potassiated composition and subsequent depotassiation is likely the best strategy going forward. These results are in qualitative agreement with the previous literature, which suggests that charged phases (TMO_2) typically prefer octahedral anion (O or S) stacking.[20,40] Apart from the single transition-metal-based system, investigating possible inclusion of multiple TMs within the P3 framework could result in better insertion host(s) for KIBs, where higher voltages arising from the presence of one TM can be combined with the stability contributed by another TM.

CONCLUSIONS

We explored the K-containing P3-type layered TMOs as potential intercalation hosts for KIBs using DFT calculations and the SCAN + U framework for describing electronic exchange and correlation. We considered six different TMOs, namely, $K_{0.5}TiO_2$, $K_{0.5}VO_2$, $K_{0.5}CrO_2$, $K_{0.5}MnO_2$, $K_{0.5}CoO_2$, and $K_{0.5}NiO_2$, and their corresponding depotassiated compositions as the candidate K-intercalation hosts. Apart from estimating the ground-state K-vacancy configuration in each TMO system considered, we evaluated the DFT-relaxed lattice parameters, topotactic average intercalation voltage, and 0 K thermodynamic stability. Additionally, we probed the nature of redox activity upon K (de)intercalation in these compounds by analyzing the electronic structure and on-site TM magnetic moments in the potassiated and depotassiated structures. In the case of P3-K_xMnO_2, we also evaluated the dynamical stability and K^+ mobility. Importantly, we find that K^+ prefers the honeycomb or zig-zag ordering in $K_{0.5}TMO_2$, irrespective of the TM, highlighting the dominance of electrostatic interactions between K^+ ions within the same layer. Our calculated voltages follow the general trend of standard reduction potentials of the TMs involved, with the low-voltage P3-K_xTiO_2 framework being more suitable as an anode and P3-K_xCoO_2 exhibiting the highest predicted voltage. Notably, we find the redox activity to be centered on the TM sites in all K_xTMO_2 systems, with negligible contribution from redox on the anionic sites. In terms of thermodynamic stability, we find all P3-$K_{0.5}TMO_2$ frameworks considered to be below the E^{hull} = 50 meV/atom threshold, indicating that synthesis of such compounds is likely to be facile. Finally, given the combination of our thermodynamic stability and average voltage estimates, we find P3-K_xCoO_2 and K_xNiO_2 as potential candidates as KIB cathodes, while K_xMnO_2 is worth exploring, given its dynamic stability and facile K^+ mobility.

ASSOCIATED CONTENT

Supporting Information

The Supporting Information is available free of charge at https://pubs.acs.org/doi/10.1021/acs.inorgchem.3c01686.

Comparison of ideal octahedral and prismatic geometry, comparison of energies of different magnetic configurations in P3-$K_{0.5}CoO_2$, compilation of calculated lattice parameters, pDOS for depotassiated P3-TMO_2, calculated on-site magnetic moments for all compounds, 0 K phase diagrams for K−TM−O ternary and TM−O binary chemical spaces, phonon DOS and thermal properties of P3-$K_{0.5}MnO_2$ and P3-MnO_2, migration energy pathway of K^+ in P3-MnO_2 and P3-$K_{0.5}MnO_2$, and details of Rouxel diagram and cationic potential model calculations (PDF)

AUTHOR INFORMATION

Corresponding Author

Gopalakrishnan Sai Gautam − *Department of Materials Engineering, Indian Institute of Science, Bengaluru, Karnataka 560012, India;* orcid.org/0000-0002-1303-0976; Email: saigautamg@iisc.ac.in

Authors

Pawan Kumar Jha − *Faraday Materials Laboratory (FaMaL), Materials Research Centre, Indian Institute of Science, Bangalore 560012, India*

Sanyam Nitin Totade − *Department of Materials Engineering, Indian Institute of Science, Bengaluru, Karnataka 560012, India*

Prabeer Barpanda − *Faraday Materials Laboratory (FaMaL), Materials Research Centre, Indian Institute of Science, Bangalore 560012, India; Helmholtz Institute Ulm (HIU), Electrochemical Energy Storage, Ulm 89081, Germany; Institute of Nanotechnology, Karlsruhe Institute of*

https://doi.org/10.1021/acs.inorgchem.3c01686
Inorg. Chem. 2023, 62, 14971−14979

Technology (KIT), Karlsruhe 76021, Germany;
orcid.org/0000-0003-0902-3690

Complete contact information is available at:
https://pubs.acs.org/10.1021/acs.inorgchem.3c01686

Notes

The authors declare no competing financial interest.

■ ACKNOWLEDGMENTS

G.S.G. acknowledges financial support from the Indian Institute of Science (IISc) Seed Grant, SG/MHRD/20/0020 and SR/MHRD/20/0013, and support from the Science and Engineering Research Board (SERB) of Government of India, under Sanction Numbers SRG/2021/000201 and IPA/2021/000007. P.B. is grateful to the Alexander von Humboldt Foundation (Bonn, Germany) for a 2022 Humboldt fellowship for experienced researchers. P.B. acknowledges financial support from the HP Green R&D Centre (Bangalore). P.K.J. and S.N.T. thank the Ministry of Human Resource Development (MHRD), Government of India, for financial assistance. P.K.J. thanks Reshma Devi for her guidance in setting up the NEB calculations. The authors also acknowledge the computational resources provided by the Supercomputer Education and Research Centre (SERC), IISc. A portion of the calculations in this work used computational resources of the supercomputer Fugaku provided by RIKEN through the HPCI System Research Project (Project ID hp220393). We acknowledge National Supercomputing Mission (NSM) for providing computing resources of 'PARAM Siddhi-AI', under National PARAM Supercomputing Facility (NPSF), C-DAC, Pune and supported by the Ministry of Electronics and Information Technology (MeitY) and Department of Science and Technology (DST), Government of India.

■ REFERENCES

(1) Armand, M.; Tarascon, J. M. Building better batteries. *Nature* **2008**, *451*, 652−657.
(2) Dunn, B.; Kamath, H.; Tarascon, J. M. Electrical energy storage for the grid: a battery of choices. *Science* **2011**, *334*, 928−35.
(3) Whittingham, M. S. History, Evolution, and Future Status of Energy Storage. *Proc. IEEE* **2012**, *100*, 1518−1534.
(4) Whittingham, M. S. Ultimate Limits to Intercalation Reactions for Lithium Batteries. *Chem. Rev.* **2014**, *114*, 11414−11443.
(5) Hosaka, T.; Kubota, K.; Hameed, A. S.; Komaba, S. Research Development on K-Ion Batteries. *Chem. Rev.* **2020**, *120*, 6358−6466.
(6) Hwang, J.-Y.; Myung, S.-T.; Sun, Y.-K. Recent Progress in Rechargeable Potassium Batteries. *Adv. Funct. Mater.* **2018**, *28*, No. 1802938.
(7) Kim, H.; Kim, J. C.; Bianchini, M.; Seo, D.-H.; Rodriguez-Garcia, J.; Ceder, G. Recent Progress and Perspective in Electrode Materials for K-Ion Batteries. *Adv. Energy Mater.* **2018**, *8*, No. 1702384.
(8) Zhang, X.; Wei, Z.; Dinh, K. N.; Chen, N.; Chen, G.; Du, F.; Yan, Q. Layered Oxide Cathode for Potassium-Ion Battery: Recent Progress and Prospective. *Small* **2020**, *16*, No. 2002700.
(9) Delmas, C.; Fouassier, C.; Hagenmuller, P. Structural classification and properties of the layered oxides. *Physica B+C* **1980**, *99*, 81−85.
(10) Delmas, C.; Devalette, M.; Fouassier, C.; Hagenmuller, P. Les phases K_XCrO_2 ($X \leqslant 1$). *Mater. Res. Bull.* **1975**, *10*, 393−398.
(11) Fouassier, C.; Delmas, C.; Hagenmuller, P. Evolution structurale et proprietes physiques des phases A_XMO_2 (A = Na, K; M = Cr, Mn, Co) ($x \leqslant 1$). *Mater. Res. Bull.* **1975**, *10*, 443−449.
(12) Han, S. C.; Park, W. B.; Sohn, K.-S.; Pyo, M. $KFeO_2$ with corner-shared FeO_4 frameworks as a new type of cathode material in potassium-ion batteries. *J. Solid State Electrochem.* **2019**, *23*, 3135−3143.
(13) Hoppe, R.; Sabrowsky, H. Oxoscandate der Alkalimetalle: $KScO_2$ und $RbScO_2$. *Z. Anorg. Allg. Chem.* **1965**, *339*, 144−154.
(14) Jansen, M.; Chang, F. M.; Hoppe, R. Zur Kenntnis von $KMnO_2$. *Z. Anorg. Allg. Chem.* **1982**, *490*, 101−110.
(15) Kim, H.; Seo, D.-H.; Urban, A.; Lee, J.; Kwon, D.-H.; Bo, S.-H.; Shi, T.; Papp, J. K.; McCloskey, B. D.; Ceder, G. Stoichiometric Layered Potassium Transition Metal Oxide for Rechargeable Potassium Batteries. *Chem. Mater.* **2018**, *30*, 6532−6539.
(16) Zhao, C.; Wang, Q.; Yao, Z.; Wang, J.; Sánchez-Lengeling, B.; Ding, F.; Qi, X.; Lu, Y.; Bai, X.; Li, B.; Li, H.; Aspuru-Guzik, A.; Huang, X.; Delmas, C.; Wagemaker, M.; Chen, L.; Hu, Y. S. Rational design of layered oxide materials for sodium-ion batteries. *Science* **2020**, *370*, 708−711.
(17) Lei, Y.; Li, X.; Liu, L.; Ceder, G. Synthesis and Stoichiometry of Different Layered Sodium Cobalt Oxides. *Chem. Mater.* **2014**, *26*, 5288−5296.
(18) Parant, J.-P.; Olazcuaga, R.; Devalette, M.; Fouassier, C.; Hagenmuller, P. Sur quelques nouvelles phases de formule NaxMnO2 ($x \leqslant 1$). *J. Solid State Chem.* **1971**, *3*, 1−11.
(19) Claude Delmas, M. M.; Fouassier, C.; Hagenmuller, P. Stabilite relative des environnements octaedrique et prismatique triangulaire dans les oxydes lamellaires alcalins A_xMO_2 ($x \leqslant 1$). *Mater. Res. Bull.* **1976**, *11*, 1483−1488.
(20) Radin, M. D.; Van der Ven, A. Stability of Prismatic and Octahedral Coordination in Layered Oxides and Sulfides Intercalated with Alkali and Alkaline-Earth Metals. *Chem. Mater.* **2016**, *28*, 7898−7904.
(21) Vaalma, C.; Giffin, G. A.; Buchholz, D.; Passerini, S. Non-Aqueous K-Ion Battery Based on Layered K0.3MnO2 and Hard Carbon/Carbon Black. *J. Electrochem. Soc.* **2016**, *163*, A1295.
(22) Kim, H.; Seo, D.-H.; Kim, J. C.; Bo, S.-H.; Liu, L.; Shi, T.; Ceder, G. Investigation of Potassium Storage in Layered P3-Type $K_{0.5}MnO_2$ Cathode. *Adv. Mater.* **2017**, *29*, No. 1702480.
(23) Bianchini, M.; Wang, J.; Clément, R. J.; Ouyang, B.; Xiao, P.; Kitchaev, D.; Shi, T.; Zhang, Y.; Wang, Y.; Kim, H.; Zhang, M.; Bai, J.; Wang, F.; Sun, W.; Ceder, G. The interplay between thermodynamics and kinetics in the solid-state synthesis of layered oxides. *Nat. Mater.* **2020**, *19*, 1088−1095.
(24) Kubota, K.; Kumakura, S.; Yoda, Y.; Kuroki, K.; Komaba, S. Electrochemistry and Solid-State Chemistry of $NaMeO_2$ (Me = 3d Transition Metals). *Adv. Energy Mater.* **2018**, *8*, No. 1703415.
(25) Hironaka, Y.; Kubota, K.; Komaba, S. P2- and P3-K_xCoO_2 as an electrochemical potassium intercalation host. *Chem. Commun.* **2017**, *53*, 3693−3696.
(26) Hwang, J.-Y.; Kim, J.; Yu, T.-Y.; Myung, S.-T.; Sun, Y.-K. Development of P3-$K_{0.69}CrO_2$ as an ultra-high-performance cathode material for K-ion batteries. *Energy Environ. Sci.* **2018**, *11*, 2821−2827.
(27) Kaufman, J. L.; Van der Ven, A. Antiphase boundary migration as a diffusion mechanism in a P3 sodium layered oxide. *Phys. Rev. Mater.* **2021**, *5*, No. 055401.
(28) Kohn, W.; Sham, L. J. Self-Consistent Equations Including Exchange and Correlation Effects. *Phys. Rev.* **1965**, *140*, A1133−A1138.
(29) Hohenberg, P.; Kohn, W. Inhomogeneous Electron Gas. *Phys. Rev.* **1964**, *136*, B864−B871.
(30) Kresse, G.; Furthmüller, J. Efficient iterative schemes for ab initio total-energy calculations using a plane-wave basis set. *Phys. Rev. B* **1996**, *54*, 11169−11186.
(31) Kresse, G.; Furthmüller, J. Efficiency of ab-initio total energy calculations for metals and semiconductors using a plane-wave basis set. *Comput. Mater. Sci.* **1996**, *6*, 15−50.
(32) Kresse, G.; Joubert, D. From ultrasoft pseudopotentials to the projector augmented-wave method. *Phys. Rev. B* **1999**, *59*, 1758−1775.
(33) Blöchl, P. E. Projector augmented-wave method. *Phys. Rev. B* **1994**, *50*, 17953−17979.

(34) Sai Gautam, G.; Carter, E. A. Evaluating transition metal oxides within DFT-SCAN and SCAN + *U* frameworks for solar thermochemical applications. *Phys. Rev. Mater.* **2018**, *2*, No. 095401.
(35) Long, O. Y.; Gautam, Sai.; Carter, G.; Evaluating, E. A. optimal *U* for 3*d* transition-metal oxides within the SCAN + *U* framework. *Phys. Rev. Mater.* **2020**, *4*, No. 045401.
(36) Monkhorst, H. J.; Pack, J. D. Special points for Brillouin-zone integrations. *Phys. Rev. B* **1976**, *13*, 5188−5192.
(37) Ho, K. M.; Fu, C. L.; Harmon, B. N.; Weber, W.; Hamann, D. R. Vibrational Frequencies and Structural Properties of Transition Metals via Total-Energy Calculations. *Phys. Rev. Lett.* **1982**, *49*, 673−676.
(38) Sun, J.; Ruzsinszky, A.; Perdew, J. P. Strongly Constrained and Appropriately Normed Semilocal Density Functional. *Phys. Rev. Lett.* **2015**, *115*, No. 036402.
(39) Anisimov, V. I.; Zaanen, J.; Andersen, O. K. Band theory and Mott insulators: Hubbard U instead of Stoner I. *Phys. Rev. B* **1991**, *44*, 943−954.
(40) Long, O. Y.; Sai Gautam, G.; Carter, E. A. Assessing cathode property prediction via exchange-correlation functionals with and without long-range dispersion corrections. *Phys. Chem. Chem. Phys.* **2021**, *23*, 24726−24737.
(41) Jha, P. K.; Singh, S.; Shrivastava, M.; Barpanda, P.; Sai Gautam, G. First principles investigation of anionic redox in bisulfate lithium battery cathodes. *Phys. Chem. Chem. Phys.* **2022**, *24*, 22756−22767.
(42) Hellenbrandt, M. The Inorganic Crystal Structure Database (ICSD)—Present and Future. *Crystallogr. Rev.* **2004**, *10*, 17−22.
(43) Ong, S. P.; Richards, W. D.; Jain, A.; Hautier, G.; Kocher, M.; Cholia, S.; Gunter, D.; Chevrier, V. L.; Persson, K. A.; Ceder, G. Python Materials Genomics (pymatgen): A robust, open-source python library for materials analysis. *Comput. Mater. Sci.* **2013**, *68*, 314−319.
(44) Momma, K.; Izumi, F. VESTA 3 for three-dimensional visualization of crystal, volumetric and morphology data. *J. Appl. Crystallogr.* **2011**, *44*, 1272−1276.
(45) Aydinol, M. K.; Kohan, A. F.; Ceder, G.; Cho, K.; Joannopoulos, J. Ab initio study of lithium intercalation in metal oxides and metal dichalcogenides. *Phys. Rev. B* **1997**, *56*, 1354−1365.
(46) Aydinol, M. K.; Kohan, A. F.; Ceder, G. Ab initio calculation of the intercalation voltage of lithium-transition-metal oxide electrodes for rechargeable batteries. *J. Power Sources* **1997**, *68*, 664−668.
(47) Sai Gautam, G.; Stechel, E. B.; Carter, E. A. Exploring Ca−Ce−M−O (M = 3d Transition Metal) Oxide Perovskites for Solar Thermochemical Applications. *Chem. Mater.* **2020**, *32*, 9964−9982.
(48) Tekliye, D. B.; Kumar, A.; Weihang, X.; Mercy, T. D.; Canepa, P.; Sai Gautam, G. Exploration of NaSICON Frameworks as Calcium-Ion Battery Electrodes. *Chem. Mater.* **2022**, *34*, 10133−10143.
(49) Sun, W.; Dacek, S. T.; Ong, S. P.; Hautier, G.; Jain, A.; Richards, W. D.; Gamst, A. C.; Persson, K. A.; Ceder, G. The thermodynamic scale of inorganic crystalline metastability. *Sci. Adv.* **2016**, *2*, No. e1600225.
(50) Togo, A.; Tanaka, I. First principles phonon calculations in materials science. *Scr. Mater.* **2015**, *108*, 1−5.
(51) Sheppard, D.; Terrell, R.; Henkelman, G. Optimization methods for finding minimum energy paths. *J. Chem. Phys.* **2008**, *128*, 128.
(52) Devi, R.; Singh, B.; Canepa, P.; Sai Gautam, G. Effect of exchange-correlation functionals on the estimation of migration barriers in battery materials. *npj Comput. Mater.* **2022**, *8*, 160.
(53) Pauling, L. *The Nature of the Chemical Bond and the Structure of Molecules and Crystals: An Introduction to Modern Structural Chemistry*; Cornell University Press, 1960.
(54) Pauling, L. The principles determining the structure of complex ionic crystals. *J. Am. Chem. Soc.* **1929**, *51*, 1010−1026.
(55) Kubota, K.; Asari, T.; Yoshida, H.; Yaabuuchi, N.; Shiiba, H.; Nakayama, M.; Komaba, S. Understanding the Structural Evolution and Redox Mechanism of a $NaFeO_2$−$NaCoO_2$ Solid Solution for Sodium-Ion Batteries. *Adv. Funct. Mater.* **2016**, *26*, 6047−6059.
(56) Kaufman, J. L.; Van der Ven, A. Na_xCoO_2 phase stability and hierarchical orderings in the O3/P3 structure family. *Phys. Rev. Mater.* **2019**, *3*, No. 015402.
(57) Toriyama, M. Y.; Kaufman, J. L.; Van der Ven, A. Potassium Ordering and Structural Phase Stability in Layered K_xCoO_2. *ACS Appl. Energy Mater.* **2019**, *2*, 2629−2636.
(58) Kaufman, J. L.; Van der Ven, A. Ordering and Structural Transformations in Layered K_xCrO_2 for K-Ion Batteries. *Chem. Mater.* **2020**, *32*, 6392−6400.
(59) Masese, T.; Yoshii, K.; Yamaguchi, Y.; Okumura, T.; Huang, Z.-D.; Kato, M.; Kubota, K.; Furutani, J.; Orikasa, Y.; Senoh, H.; Sakaebe, H.; Shikano, M. Rechargeable potassium-ion batteries with honeycomb-layered tellurates as high voltage cathodes and fast potassium-ion conductors. *Nat. Commun.* **2018**, *9*, No. 3823.
(60) Rong, Z.; Malik, R.; Canepa, P.; Sai Gautam, G.; Liu, M.; Jain, A.; Persson, K.; Ceder, G. Materials Design Rules for Multivalent Ion Mobility in Intercalation Structures. *Chem. Mater.* **2015**, *27*, 6016−6021.
(61) Yabuuchi, N.; Kubota, K.; Dahbi, M.; Komaba, S. Research Development on Sodium-Ion Batteries. *Chem. Rev.* **2014**, *114*, 11636−11682.
(62) Goodenough, J. B.; Mizushima, K.; Takeda, T. Solid-Solution Oxides for Storage-Battery Electrodes. *Jpn. J. Appl. Phys.* **1980**, *19*, 305.

https://doi.org/10.1021/acs.inorgchem.3c01686
Inorg. Chem. 2023, 62, 14971−14979